Environmental Science & Technology

pubs.acs.org/est

Article

Accumulation of Soil Microbial Necromass Controlled by Microbe−Mineral Interactions

Qian Zhao, Sheryl Bell, Ravi Kukkadapu, Jocelyn Richardson, John Cliff, Mark Bowden, Sarah Leichty, and Kirsten S. Hofmockel*

Cite This: https://doi.org/10.1021/acs.est.5c01482

Read Online

ACCESS | Metrics & More | Article Recommendations | Supporting Information

ABSTRACT: Soil organic matter (SOM) is a key reservoir for global carbon (C), supporting soil fertility and influencing greenhouse gas emissions. Microbial residues, composed of dead cells and cellular fragments, are major contributors to SOM formation. Yet, mechanisms by which minerals enhance the accumulation of microbial residues remain poorly understood. Here, we used ^{13}C-labeled glucose in a year-long incubation to trace microbial residue in sandy and silty soils. Across both soils, approximately 89% of retained microbial ^{13}C was recovered in the fine (<53 μm) mineral-associated organic matter (MAOM) pool. Within this pool, the light MAOM fraction, enriched in poorly crystalline Fe minerals, held 4.3 times more ^{13}C than the heavy, phyllosilicate-dominated MAOM fraction, despite accounting for only 17.2% of the total MAOM mass and 12.3% of the total soil mass. Along with ^{13}C enrichment, the light MAOM fraction showed greater abundance of N-containing groups, e.g., (amides and amino groups), indicative of microbial-derived compounds like proteins and amino sugars. Fe oxides in light MAOM from both soils were spatially dispersed. Microbial residue accumulation was greater in finer-textured silty soil. These findings demonstrate that mineral composition and texture jointly regulate microbial necromass accrual, highlighting light MAOM as a key pool for enhancing soil C storage.

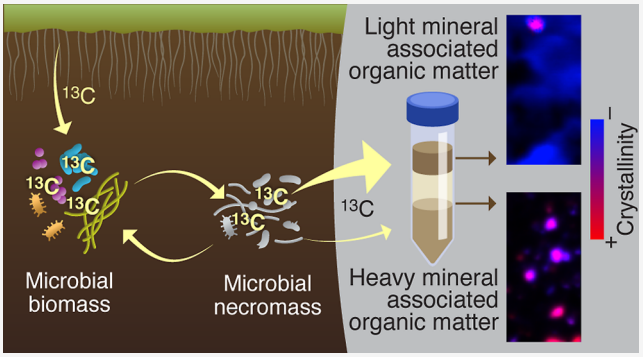

KEYWORDS: *microbial necromass, mineral-associated organic matter (MAOM), amorphous iron oxide, soil organic matter (SOM), carbon persistence, ^{13}C isotope labeling, microbe−mineral interactions, bioenergy cropping system*

1. INTRODUCTION

Soil organic matter (SOM) is crucial to sustaining ecosystem processes and regulating atmospheric CO_2 concentrations.[1] While the role of plant residues in SOM persistence has long been recognized;[2,3] recent research emphasizes the importance of microbial residues (collectively referred to as microbial necromass) as a major contributor to the slowly cycling SOM pool.[2,4,5] Microbial necromass contributes to 33−62% of total soil organic carbon (SOC) across diverse ecosystems (measured as amino sugars).[6,7] Thus, it is important to understand the mechanisms governing the accumulation of microbial necromass carbon (C) across soils.

Microbial residues preferentially persist in fine-textured soils via microbe−mineral interactions, whereas in coarsely textured soils, which contain more crystalline or primary minerals, the stabilization of microbial necromass depends more on microbial processing than on abiotic adsorption.[4,8] Beyond soil texture, microbial necromass persistence often involves interactions with specific mineral phases,[8−10] contributing to the mineral-associated organic matter (MAOM) pool with mean residence times of decades to centuries.[11,12] Among mineral types, poorly crystalline iron (Fe) and aluminum (Al) (hydroxy)oxides and aluminosilicates (e.g., allophane) exhibit high sorption capacities for organic matter (OM) due to their high surface areas and reactive hydroxyl-rich surfaces.[13,14] Their abundance is positively correlated with SOC across soils.[9,15,16] Given that microbial residues constitute a substantial portion of SOC,[2,4−7] and SOC is positively correlated with poorly crystalline minerals across soils,[9,15,16] we need to understand how specific mineral phases contribute to necromass accumulation and the development of healthy soils.

The molecular diversity of microbial necromass, and SOM in general, introduces uncertainty in organo-mineral interactions,[9,17] affecting predictions of necromass persistence. Nitrogen (N)-rich microbial molecules, such as amino sugars and peptides, and carboxylic-rich molecules preferentially

Received: January 30, 2025
Revised: July 8, 2025
Accepted: July 9, 2025

associate with poorly crystalline minerals.[18−21] While studies using synthetic minerals (e.g., amorphous Al hydroxide) show strong abiotic sorption of microbial necromass,[8] the contribution of these mineral phases to microbial necromass accumulation in native soil, where minerals exist in complex matrices, remains poorly resolved.

Recent efforts to characterize MAOM commonly define it as the <53 μm fraction.[23−26] However, this size-based definition can overestimate MAOM mass by including minerals with minimal OM. Previous studies suggest that fractions with densities >2.4 g/cm^3 are dominated by quartz and Fe-bearing silicates with little OM, whereas fractions <2.4 g/cm^3 contain more reactive clays and organic-rich phases.[27−31] To improve specificity, we coupled size separation with density fractionation to differentiate organo-mineral complexes from nearly bare mineral particles, producing light and heavy MAOM fractions.

While some studies have examined plant-derived C across these density pools,[27,30] little is known about the microbial contributions. We hypothesized that microbial necromass is primarily stabilized in the light MAOM fraction, whereas the heavy MAOM fraction consists of minerals with limited organics. To test these hypotheses, we used ^{13}C-labeled glucose in native soils to trace microbial residue incorporation into SOM fractions. We examined two contrasting soils (sandy vs silty loam) and two cropping systems (corn vs switchgrass) to evaluate the influence of texture and management on microbial necromass accumulation.[32,33] By integrating isotope tracing with mineralogical separation, we aim to clarify how mineral phases regulate microbial necromass accumulation in soil. This mechanistic understanding can enhance predictive models of soil C persistence and inform C sequestration strategies in managed ecosystems.

2. MATERIALS AND METHODS

2.1. Experimental Site and Soil Sampling. Samples were collected from switchgrass (*Panicum virgatum* L.) and corn (*Zea mays* L.) plots at the Arlington Agricultural Research Station (AARS), the University of Wisconsin−Madison (43°18′N, 89°20′W) and the W.K. Kellogg Biological Station (KBS) Long-Term Ecological Research Site (42°24′N, 85°24′W), as part of the Great Lakes Bioenergy Research Center (GLBRC) Intensive Biofuel Cropping System Experiments. Both sites have continental meteorology, with mean annual precipitation and temperature of 810 mm and 9.7 °C at AARS and 833 mm and 7.4 °C at KBS. Soil texture varies between sites: KBS has a sandy loam (Kalamazoo series, mesic Typic Hapludalf; 63% sand, 31% silt, 6% clay), while AARS has a silty loam (Plano series, mesic Typic Argiudoll; 9% sand, 66% silt, 25% clay).[34,35] The sandy loam has lower total soil C and N (1.43% C, 0.13% N) than the silty loam (2.24% C, 0.21% N) as sandy loam has a slightly lower pH (6.1) than silty loam (6.6).[36] pH was measured by mixing dry soil with deionized water at a ratio of 1:2.[36] Fertilization is based on spring soil tests, averaging 167 kg of N ha^{-1} y^{-1} as urea-ammonium nitrate in corn and 56 kg of N ha^{-1} y^{-1} in switchgrass plots.

Two soils with contrasting soil textures were selected to determine whether the soil texture and mineralogy regulate microbial necromass accumulation. At each site (AARS and KBS), two cropping systems, perennial switchgrass and annual no-until corn, were established in 40 × 28 m plots to examine cropping system effects. Aboveground biomass is harvested annually, leaving ∼10 cm stubble for corn and ∼15 cm for switchgrass.[36] Soil was collected in April 2018, 10 years after the cropping treatments were established and the last occurrence of tillage. Samples were collected using a 5 cm diameter core to a depth of 15 cm, and the 5−15 cm increment was used to represent bulk soil while reducing surface litter heterogeneity. By limiting additional C inputs via plant litter, we increased microbial assimilation of the ^{13}C tracer, promoting recycling and the mineralization of microbial residues over time. Three replicated cores per site and cropping system were collected prior to spring fertilizer application or corn planting. Soils were packed in sealed plastic bags, shipped on ice, and sieved to 2 mm mesh, and roots were removed. Field-moist soil was stored in sealed Pyrex containers at 4 °C until further analyses.

2.2. Incubation Design and Sampling. Laboratory incubations consisted of 125 g of 2 mm-sieved field soil placed in 236 mL wide-mouth mason jars and amended with either (99 at. % universally labeled) ^{13}C glucose or natural abundance (1.09 at. %) glucose in solution at a rate of 100 μg C per gram dry soil. Incubations were maintained at 15 °C for 12 months (Figure 1). While glucose represents a labile C source, it was chosen to promote microbial assimilation and maximize incorporation into necromass during early transformation stages. This approach enables high-resolution isotopic tracing of microbial residue dynamics and complements studies using more complex plant-derived C sources. Although individual cells have a high turnover from hours to days, community-level C turnover is estimated at 30 −50 days;[37,38] thus, our year-long incubation reflects longer-term persistence of microbial residues. Our previous work from the same incubation experiment showed rapid microbial assimilation and respiration after glucose addition, using respiration, compound-specific isotope analysis, and phospholipid fatty acid (PLFA) profiling.[39] On average, 15.7% of the added ^{13}C glucose was respired within 24 h, with only 42% remaining in soil after one year. The remaining label was detected in microbial residues, including metabolites, lipids, and proteins.[39] ^{13}C PLFA confirmed redistribution of the ^{13}C label beyond fast-growing microbes to a broader microbial community, with incorporation into both bacteria and fungi.[39] We acknowledge that ^{13}C glucose may not completely transform to microbial residues due to abiotic sorption to minerals. Nonetheless, this multimethod evidence suggests that

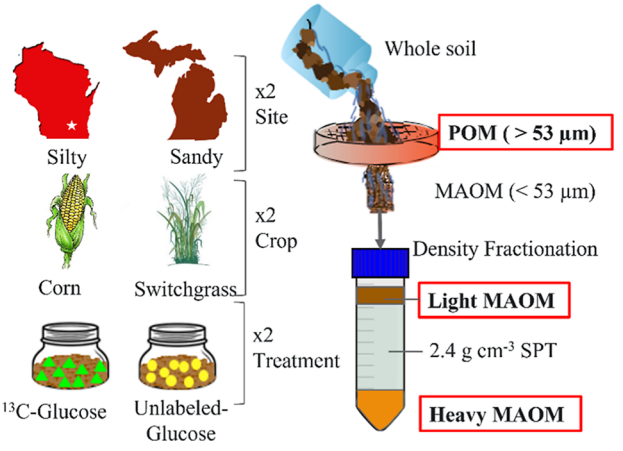

Figure 1. Experimental design of field treatment, isotopic incubation, and fractionation approach.

https://doi.org/10.1021/acs.est.5c01482
Environ. Sci. Technol. XXXX, XXX, XXX−XXX

most ^{13}C labeled glucose, excluding the loss to respiration, was processed through microbial assimilation, turnover, and ultimately accumulated in MAOM. Although we did not directly separate live versus dead biomass at the final time point, these results support the interpretation that the majority of retained ^{13}C after one year largely represents microbial residues. The distribution of labeled C across soil fractions is presented in the Results.

Microcosms were wet to 60% water-filled pore space (WFPS) on a three-week cycle (rewet to 60% WFPS on two consecutive weeks and then allowed to dry down on the third week) to induce C cycling and turnover through rewetting and drying events.[40,41] To avoid contamination and reduce evaporation while allowing air exchange, jars were capped with a modified lid that was drilled with a 7 mm hole that was covered with a 1.2 μm filter. Soil from incubation jars were homogenized and harvested 365 days after glucose addition.

2.3. Size and Density Fractionation. In native soils, minerals exist in a heterogeneous matrix of organo-organic, organo-mineral complexes, and nearly bare mineral gains, making it challenging to isolate specific microbe−mineral interactions. To resolve this complexity, we applied a size and density fractionation approach to physically isolate SOM pools differing in mineralogy and OC content. Size-based separation alone, commonly defining all particles <53 μm as MAOM, can overestimate MAOM mass by including minerals with minimal OM.[23−26] To improve resolution, we used size separation first followed by a density fractionation, which resulted in two distinct MAOM fractions: the light MAOM (organo-mineral complexes) and heavy MAOM (nearly bare minerals with limited OM). By separating light and heavy MAOM fractions, we characterized the distinct mineralogy as well as quantified microbial necromass accumulations from the two MAOM fractions. The novelty of this fractionation approach is to emphasize the differentiation of mineral phases that preferentially adsorb necromass C, which is not typically addressed in other studies in field soil. While we acknowledge that microbial residues may associate with sand surfaces in the POM fraction, we predict that in the soils used in our study, this contribution is generally negligible compared to OM associated with finer particles (silt and clay).

Soil samples were sieved to 2 mm, air-dried, and dispersed in deionized water by adding glass beads and shaking at 200 rpm for 18 h. The sample was poured over a 53 μm sieve to separate MAOM (<53 μm, silt- and clay-sized) from POM (>53 μm, sand-sized particles and plant detritus) by wet sieving (Figure 1). Before further separating MAOM fractions, dissolved organic carbon (DOC) was removed by centrifuging the wet sieved MAOM fraction for 10 min at 4000 rpm. A subsample of DOC was saved and analyzed for C concentration and ^{13}C enrichment. The MAOM fraction was resuspended within 2.4 g cm^{-3} sodium polytungstate (SPT) and shaken for 20 min at 4000 rpm to separate organo-mineral complexes (light) from bare clay minerals and metal oxides (heavy) (Figure 1).[27,28,42] The light MAOM fraction was decanted into a new tube. Both light and heavy MAOM fractions were rinsed with deionized water and rinsed three times to remove the residual SPT solution. Light and heavy MAOM fractions were separated for subsequent analyses to quantify the C content and characterize mineralogy.

2.42.4. Isotope Ratio Mass Spectrometry Analysis. Dried whole soil, POM, light, and heavy MAOM fractions were individually encapsulated in tin and analyzed for ($\delta^{13}C$) using a Costech Analytical (Valencia, CA) Elemental Analyzer (EA, ECS 4010 CHNSO Analyzer) coupled to a Thermo Scientific (Bremen, Germany) Delta V Plus IRMS. Samples were combusted at 1020 °C in an EA reactor (loaded with cobaltic oxide and chromium oxide catalyst) and subsequently reduced (with copper catalyst) at 650 °C. A 2-point data correction[43] was conducted using in-house glutamic acid isotope samples calibrated against USGS-40 and USGS-41 ($\delta^{13}C$ of −26.39‰ and +37.63‰, respectively). Data were reported as

$$\delta^{13}C\ (‰) = \left(\frac{R_{sample}}{R_{standard}} - 1\right) \times 1000$$

where R is the $^{13}C/^{12}C$ ratio in the samples and international standard Vienna Pee Dee Belemnite ($R_{V\text{-}PDB}$ = 0.0112372).

The whole soil and each fraction of all samples were analyzed for total carbon/total nitrogen (TC/TN) contents on a Vario EL cube elemental analyzer (Elementar Langenselbold, Germany). Samples were first freeze-dried and ground in a ball mill (Retsch MM400) with 2.3 mm stainless steel beads to improve the accuracy of the measurements.

2.5. Mineralogy Analyses. Powder X-ray diffraction (XRD) and ^{57}Fe−Mössbauer spectroscopy were conducted to determine the mineral composition in light and heavy MAOM fractions. For XRD, air-dried soil powder (ca. 50 mg) was loaded into a zero-background holder. Diffraction patterns were measured by a Rigaku SmartLab SE diffractometer operated at 40 keV and 44 mA using Cu Kα radiation. Samples were scanned from 2° to 100° at 0.01° intervals using a D/Tex 250 position-sensitive detector. Crystalline phases were identified by matching diffraction patterns to reference data from the International Center for Diffraction Data.

Variable-temperature ^{57}Fe−Mössbauer spectra were collected by using a WissEl Elektronik or a Web Research instrument, both equipped with a closed-cycle SHI-850 cryostat (Janis Research Co., Inc.), a Sumitomo CKW-21 He compressor, and an Ar−Kr proportional counter detector (LND, Inc.). Samples (∼100−150 mg) were prepared by mixing with powdered sugar following Peretyazhko et al.[44] Spectra were modeled using a Voigt-based hyperfine distribution in Recoil[45] (University of Ottawa) to quantify Fe species. Bulk concentrations of individual Fe phases were estimated by multiplying their Mössbauer-derived relative abundance by total Fe content, measured separately by microwave digestion and ICP-OES, which allows us to assume the soil is free of magnetite. We multiplied proportions of each Fe mineral phase by the total Fe content of each sample to have the estimated Fe concentrations of each Fe mineral phase. Magnetite was assumed to be absent in all of the samples.

2.6. Nanoscale Secondary Ion Mass Spectrometry Analysis. NanoSIMS was used to determine the spatial distribution of ^{13}C-labeled microbial necromass in light and heavy MAOM fractions from sandy and silty soils. Samples from the 12 month incubation with either ^{13}C-labeled or natural abundance glucose were analyzed using a Cameca NanoSIMS 50L at the Environmental Molecular Sciences Laboratory. Following Mueller et al.,[46] a 2 μL aliquot of a ∼ 1:20,000 soil/water suspension was pipetted onto a conductive silicon wafer, dried in a desiccator, and coated with 20 nm of high-purity gold. Reflected light and scanning electron microscopy (SEM) images were taken to identify regions of interest (ROIs). NanoSIMS imaging was conducted with a 16

https://doi.org/10.1021/acs.est.5c01482
Environ. Sci. Technol. XXXX, XXX, XXX−XXX

keV Cs^+ primary ion beam at 512 × 512-pixel resolution. Secondary ions were accelerated to 8 keV and detected using electron multipliers. For $^{13}C/^{12}C$ analysis, 45 × 45 μm areas were presputtered with 1×10^{16} ions cm^{-2} before collecting $^{12}C_2^-$, $^{12}C^{13}C^-$, and $^{12}C^{14}N^-$ ions using a 2 pA primary beam (~120 nm diameter) and 13.5 ms px^{-1} dwell time. Other analytical conditions include a 300 μm D1 aperture, a 30 μm entrance slit, a 200 μm aperture slit, and a 90 μm exit slit. Peak centering and abundance sensitivity were monitored between analyses, with special attention to the $^{12}C^{13}C^-$ peak relative to $^{12}C_2^-H^-$. Images were processed using the OpenMIMS plugin for ImageJ, correcting for dead time (44 ns) and QSA (β = 0.5). ROIs were manually drawn based on $^{12}C_2^-$ and $^{12}C^{14}N^-$ ion images and $^{12}C^{13}C^-/^{12}C_2^-$ HSI images to target organic-C-rich hotspots. Data from the ROIs were exported to a custom spreadsheet for data reduction. Quantitative $^{13}C/^{12}C$ ratios were calibrated against an in-house yeast standard ($\delta^{13}C$ = −10.967 ± 0.18‰, $\bar{X}$ ± 1SD, n = 28, VPDB) run during the same session under matched conditions. Standard error propagation included contributions from counting statistics, variation among 16 yeast reference cells, and uncertainty in bulk yeast $\delta^{13}C$ relative to the VPDB.

2.7. Synchrotron XRF Imaging and XANES Spectroscopy. Synchrotron μ-X-ray Fluorescence (μ-XRF) and X-ray Absorption Near Edge Structure (XANES) spectroscopy were used to determine the spatial distributions of Fe mineral phases in light and heavy MAOM fractions from two soils. μ-XRF and XANES data were collected on beamlines 2−3 at the Stanford Synchrotron Radiation Lightsource (SSRL), SLAC National Accelerator Laboratory. Beamline 2−3 is an X-ray microprobe equipped with a water-cooled double Si (111) monochromator and a single-element Hitachi Vortex 90EX detector. The monochromator was calibrated to the Fe K-edge using the first inflection point of an Fe metal foil at 7112.0 eV. Analyses were performed under standard ring conditions (3 GeV, ~500 mA) at ambient air temperature. Total Fe maps of each MAOM fraction from the two sites were obtained at a 5 μm resolution at 7200 eV, slightly above the Fe K-edge. To resolve Fe speciation, multiple-energy maps were collected at higher resolution (1 μm) at energies selected from preliminary μ-XANES spectra and literature values: 7115.2, 7126.0, 7132.0, 7133.0, and 7134.0 eV.[47]

XANES spectra were processed in SIXpack[48] and Athena.[49] Repeat spectra were averaged in SIXpack and normalized in Athena by fitting a linearized pre-edge and a second order polynomial to the postedge. End-member spectra (i.e., those most distinct and representative across the sample set) were selected by performing a principal component analyses in SIXpack. Fe phases corresponding to the end-member XANES spectra were identified by linear combination fitting using in-house Fe XANES standards from SSRL. Images were processed in the MicroAnalysis Toolkit,[50] beginning with a blurring function, which applies a Gaussian distribution function to a 5 by 5 pixel area. Maps of crystalline versus noncrystalline Fe phases were generated by applying a least-squares fitting of the end-member XANES spectra to the multiple-energy maps.

2.8. X-ray Photoelectron Spectroscopy Analysis. The C chemistry of microbial necromass between light and heavy MAOM fractions was analyzed by XPS. The sample was measured by a Physical Electronics Quantera Scanning X-ray Microprobe (Physical Electronics, Germany), which uses a focused monochromatic Al Kα (1486.7 eV) source for excitation. XPS spectra of C 1s were measured at a normal angle, with respect to the plane of the surface. Binding energies were determined with an accuracy of ±0.2 eV and calibrated using the C 1s peak at 284.86 eV. Deconvolution of C 1s spectra was done with the CasaXPS software package. The binding energy of C 1s XPS was assigned at 284.6 eV for C═C, 285 eV for C−C/C−H, 286.2 eV for C−O, 286.7 eV for C−O−C, 287.6 eV for C═O, and 289.1 eV for COO.[51−53] The averages and standard errors were calculated from four replicates from two sites and two cropping systems from each site (n = 4).

2.9. Carbon Saturation Determination. Carbon saturation for mineral-associated organic carbon (MOC_{max}) was estimated following the method outlined by Georgiou et al.,[26] a well-documented approach for assessing mineral C capacity.[54] For 2:1 clay-dominated soils, mineral adsorption capacities range from 81 to 86 g C kg^{-1} silt + clay: Feng et al.[55] reported 84 ± 4 g C kg^{-1}; Georgiou et al.[26] estimated 86 ± 9 g C kg^{-1}; and Matus[56] estimated 81 g C kg^{-1}. For 1:1 clay-dominated soils, estimates were lower and more consistent: 43 ± 4 g C kg^{-1}[55] and 48 ± 6 g C kg^{-1},[26] averaging to 46 ± 4 g C kg^{-1} silt + clay. A recent study estimated a feasible upper limit of 55 g MAOC kg^{-1} clay + silt under typical agricultural management.[57] Because of diverse mineralogy at both sites (Supplementary Figure S1), we used the average of mineral capacities between high-activity mineral (HM) and low-activity mineral (LM) from Georgiou et al.,[26] which is 67 mg C g^{-1} mineral. This value was applied to both soils, as their relative mineral phase abundances were similar (Supplementary Figure S1).

$$\text{Clay and Silt (CS)\%} = \frac{(\text{mass of light MAOM} + \text{mass of heavy MAOM})}{\text{mass of whole soil}} \times 100\%$$

where the sum of masses of light and heavy MAOM fractions is the sum of masses of clay and silt, as we separated the MAOM fraction by less than 53 μm particle size.

$$MOC_{max}\left(\frac{\text{mgC}}{\text{g}}\text{soil}\right) = \text{mineral capacity} \times CS(\%)$$

where the mineral capacity is 67 mg of C/g of mineral for all samples.

$$\text{C saturation (\%)} = \frac{MOC}{MOC_{max}} \times 100\%$$

where MOC is the total organic carbon content of light and heavy MAOM combined.

2.10. Data and Statistical Analysis. The mass of ^{13}C excess (μg ^{13}C/g soil) after one-year incubation was quantified by subtracting ^{13}C mass in the labeled sample from ^{13}C mass in paired natural abundance sample to account for background ^{13}C

$$^{13}C_{atom\%} = \frac{(\delta^{13}C + 100) \times R_{V-PDB}}{(\delta^{13}C + 100) \times R_{V-PDB} + 1} + 100\%$$

where $R_{V\text{-}PDB}$ is the $^{13}C/^{12}C$ ratio in the international standard Vienna Pee Dee Belemnite ($R_{V\text{-}PDB}$ = 0.0112372). $\delta^{13}C$ was measured by IRMS for each sample.

https://doi.org/10.1021/acs.est.5c01482
Environ. Sci. Technol. XXXX, XXX, XXX−XXX

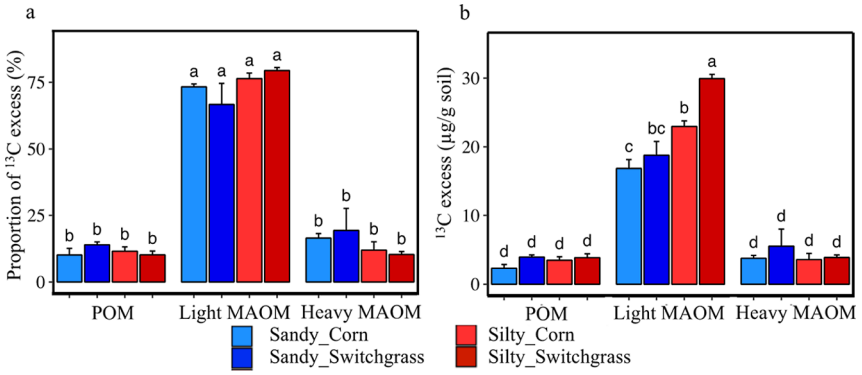

Figure 2. (a) Proportion of ^{13}C excess in each fraction relative to ^{13}C excess in the whole soil. The sum of ^{13}C excess for POM, light MAOM, and heavy MAOM was 100% ± 11.3%; (b) mass of ^{13}C excess in μg per g of soil in each soil fraction from two sites and two cropping systems. Error bars from both panels represent standard errors of three replicates from the same site, cropping system, and fraction. Means not sharing any letter are significantly different (Tukey's HSD, $p < 0.05$).

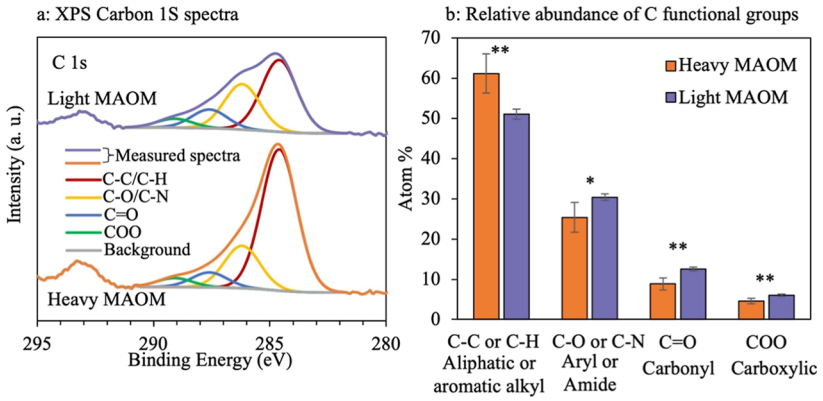

Figure 3. (a) Representative XPS carbon 1s spectra of light MAOM and heavy MAOM fractions of silty soil with switchgrass cropping system. The spectra were fitted by four components, corresponding to C functional groups. (b) The relative abundance (atom %) of C functional groups between light MAOM and heavy MAOM based on the modeled C 1s spectra. Error bars in panel b represent standard errors of four replicates from two sites and two cropping systems from each site ($n = 4$). Statistical differences are shown as "*" $0.01 < p < 0.05$, "**" $0.001 < p < 0.01$, and "***" $p < 0.001$.

$$^{13}\text{C excess}\left(\mu\text{g}\frac{^{13}\text{C}}{\text{g}}\text{soil}\right) = \frac{(^{13}C_{\text{atom\%}})_{\text{label}} - (^{13}C_{\text{atom\%}})_{\text{NA}}}{100} \times \text{C content}$$

where the C content is the C content of each labeled sample. The proportions of ^{13}C excess in each fraction were calculated by taking the mass of ^{13}C excess in each fraction (μg ^{13}C/g soil in POM, light MAOM, or heavy MAOM) after one-year incubation, divided by the sum of masses of ^{13}C excess from three fractions (μg ^{13}C/g soil). The sum of the proportions of ^{13}C excess in three fractions was 100% ± 11.3%. The mass of ^{13}C excess in C basis (μg ^{13}C/mg C) was calculated by dividing the mass of ^{13}C excess (μg ^{13}C/g soil) by C content (mg C/g soil).

All statistical tests were conducted using R software.[58] Three-way analysis of variance (ANOVA) and Tukey's HSD test at a confidence level of 95% were used with the "aov" function from the "stats" package[58] to assess the effect of soil (sandy vs silty loam), cropping system (annual vs perennial), and soil fraction (POM, light MAOM, and heavy MAOM) on the proportion of ^{13}C excess in each fraction, the mass of ^{13}C excess in μg ^{13}C/mg C and in μg ^{13}C/g soil, and the total C content (mg C/g soil). Differences in the relative abundance (atom %) of each C functional group between light and heavy MAOM fractions were tested with a *t*-test. To test significant relationships between ^{13}C atom % and $^{12}C^{14}N/^{12+13}C_2$ ratio of all ROIs from multiple areas NanoSIMS imaging, a linear regression was fitted using the "lm" function from the "stats" package[58] to only ROIs from enriched samples as the ^{13}C atomic % of ROIs from natural abundance samples are close to 1%.

3. RESULTS

3.1. Microbial Necromass Mass Distributions and Carbon Chemistry. By tracing microbial cell turnover and soil microbial products and residues (i.e., microbial necromass) with ^{13}C enrichment, we showed that the microbial necromass produced during our year-long incubation contributed substantially to the MAOM pools. An average of 88.5% (±3.0%) of the ^{13}C that remained in the soil after one year was recovered in the fine (<53 μm) MAOM fraction (Figure 2a). Our results show that the light MAOM fraction, a component of MAOM pool, was dominated by ^{13}C accumulation (Figure 2a; $F(2, 24) = 362.05$, $p < 0.001$) and accumulated 4.3 times more ^{13}C labeled microbial residues (μg ^{13}C excess/g soil) than the heavy MAOM fraction and 5.5 times more than the POM fraction (Figure 2b). Although the light MAOM fraction has a significantly greater native C content compared with

https://doi.org/10.1021/acs.est.5c01482
Environ. Sci. Technol. XXXX, XXX, XXX−XXX

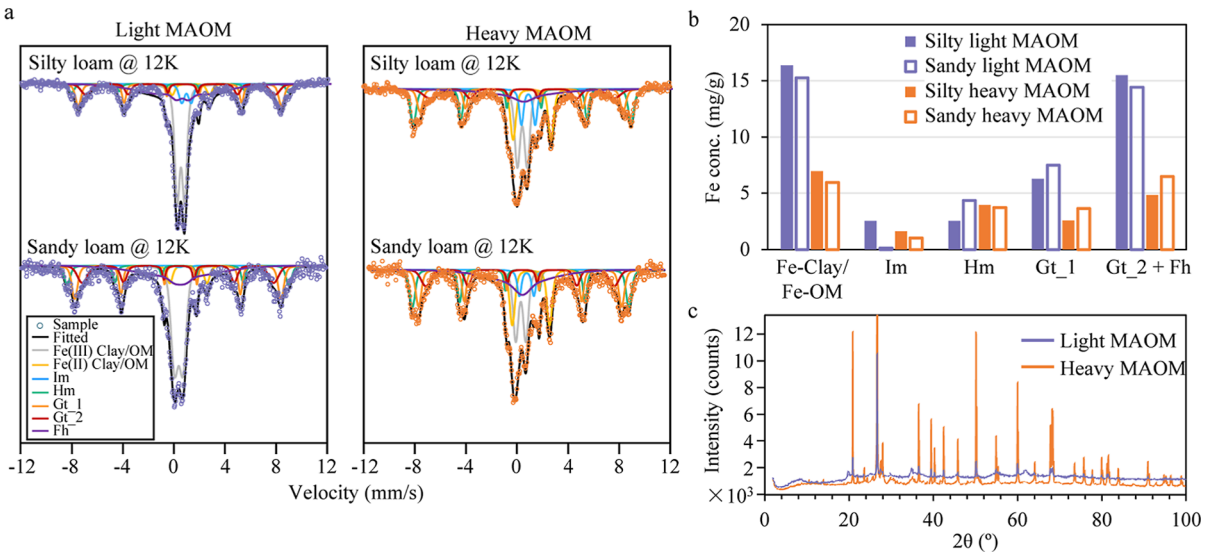

Figure 4. (a) Modeled Mössbauer spectra of the light and heavy MAOM fractions from the sandy loam measured at 12 K. (b) Fe concentrations of each Fe mineral phase from both light and heavy MAOM fractions of both soils based on modeled Mössbauer results and total Fe contents, Clay/OM or Fe-Clay/Fe-OM = Fe in clay minerals or Fe complexes with OM, Im = Fe in ilmenite, Hm = hematite, Gt_1 = nanogoethite_1, Gt_2 = nanogoethite_2, and Fh = ferrihydrite-like. The sum of Gt_2 and Fh (Gt_2 + Fh) in panel b represents disordered, poorly crystalline Fe mineral phases. Model parameters of Mössbauer spectra at 12K are included in Supplementary Table S2. (c) XRD patterns of the light and heavy MAOM fractions from the sandy loam.

POM and heavy MAOM fractions (Supplementary Figure S2a; $F(2, 24) = 117.4$, $p < 0.001$) and its soil mass only accounted for an average of 17.2% of total MAOM mass and 12.3% of total soil mass (Supplementary Figure S2c), the light MAOM fraction had significantly greater recovered ^{13}C mass on a total C basis (Supplementary Figure S2b; $F(2, 24) = 20.4$, $p < 0.001$) and absolute ^{13}C mass in μg (Supplementary Figure 2d; $F(2, 24) = 327.2$, $p < 0.001$) than POM and heavy MAOM. The difference between fractions was more pronounced in sandy loam than silty loam. The sandy loam retained a significantly smaller mass of microbial necromass in light MAOM (μg ^{13}C/g soil) (Figure 2b, $p < 0.001$) compared to the silty loam light MAOM, indicating the lower capacity of accruing necromass in sandy loam of this experiment. However, when normalized by soil C, both the light and heavy MAOM fractions of the sandy loam were more enriched with microbial necromass compared to the silty loam fractions in this study (Supplementary Figure S2b, $p < 0.001$ for both light and heavy MAOM fractions). This was supported by the lower original C loading and potentially shorter C retention times (Supplementary Figure S3) that lead to a higher availability of active sites on mineral surfaces for accruing newly produced microbial necromass in the sandy compared silty loam from this experiment. No cropping system effects were found on the excess ^{13}C fraction and mass (Figure 2).

Surface C chemistry analyzed by XPS revealed that the light MAOM fraction had relatively higher abundances of aryl or amide (C−O or C−N), carbonyl (C═O), and carboxyl (COO) groups and lower abundances of C−C or C−H groups on the top 10 nm of the sample surface than heavy MAOM (Figure 3a,b). Because ^{13}C predominantly accumulated on the mineral or soil particle surface, the higher abundances of aryl, carbonyl, and carboxyl groups in the light MAOM fraction are likely the result of newly generated microbial residues. In particular, the elevated C−N signals, primarily attributed to amide bonds, are consistent with microbial-derived compounds such as peptides and amino sugars. Similarly, the abundance of carboxyl C reflects the presence of amino acids, which are important for microbial growth, remodeling microbial cell walls, and spore germination.[59] We acknowledge that not all the surface C was microbial necromass given the small contributions of microbial necromass relative to the native C (Supplementary Figure S2b). Although XPS analysis does not provide isotopic information for determining the C chemistry of labeled microbial necromass directly, differences in labeled C mass distributions between MAOM fractions allow us to predict the C chemistry of microbial necromass accumulated in light MAOM by coupling XPS with IRMS analysis.

To further confirm that the accumulated C was of microbial origin, our study determined C/N ratios according to the bulk elemental composition in POM, light MAOM, and heavy MAOM fractions of soil samples. Regardless of soil sites and cropping systems, the average C/N ratio in the heavy MAOM fraction was 5.4 (Supplementary Figure S4), which is within a typical range of microbial origin from 5 to 8.[60] Although the C/N ratios of the light MAOM fraction (ranging from 8.6 to 9.9) were a little higher than that in the heavy MAOM fraction, it could possibly be a result of the C/N ratios of native C that partially originated from plant-derived C. A relatively high C/N ratio at 11.7 was found in the POM fraction of the silty loam, which originated from plant-derived C (Supplementary Figure S4). The C/N ratio in the POM fraction of the sandy loam was an average of 7.9, which is comparable to the ratio in the LMAOM fraction (Supplementary Figure S4). The C/N ratios in each fraction suggest that the microbial origin of C in the light MAOM fraction coincides with the enrichment of ^{13}C in the light MAOM fraction.

3.2. Mineralogy of MAOM Fractions. Significant differences in mineralogical composition between light and heavy MAOM fractions correspond with differences in microbial necromass accumulation. Mössbauer spectroscopy results revealed different proportions of the same suite of minerals in light and heavy MAOM fractions ($F = 107.3$, $p < 0.001$;

https://doi.org/10.1021/acs.est.5c01482
Environ. Sci. Technol. XXXX, XXX, XXX−XXX

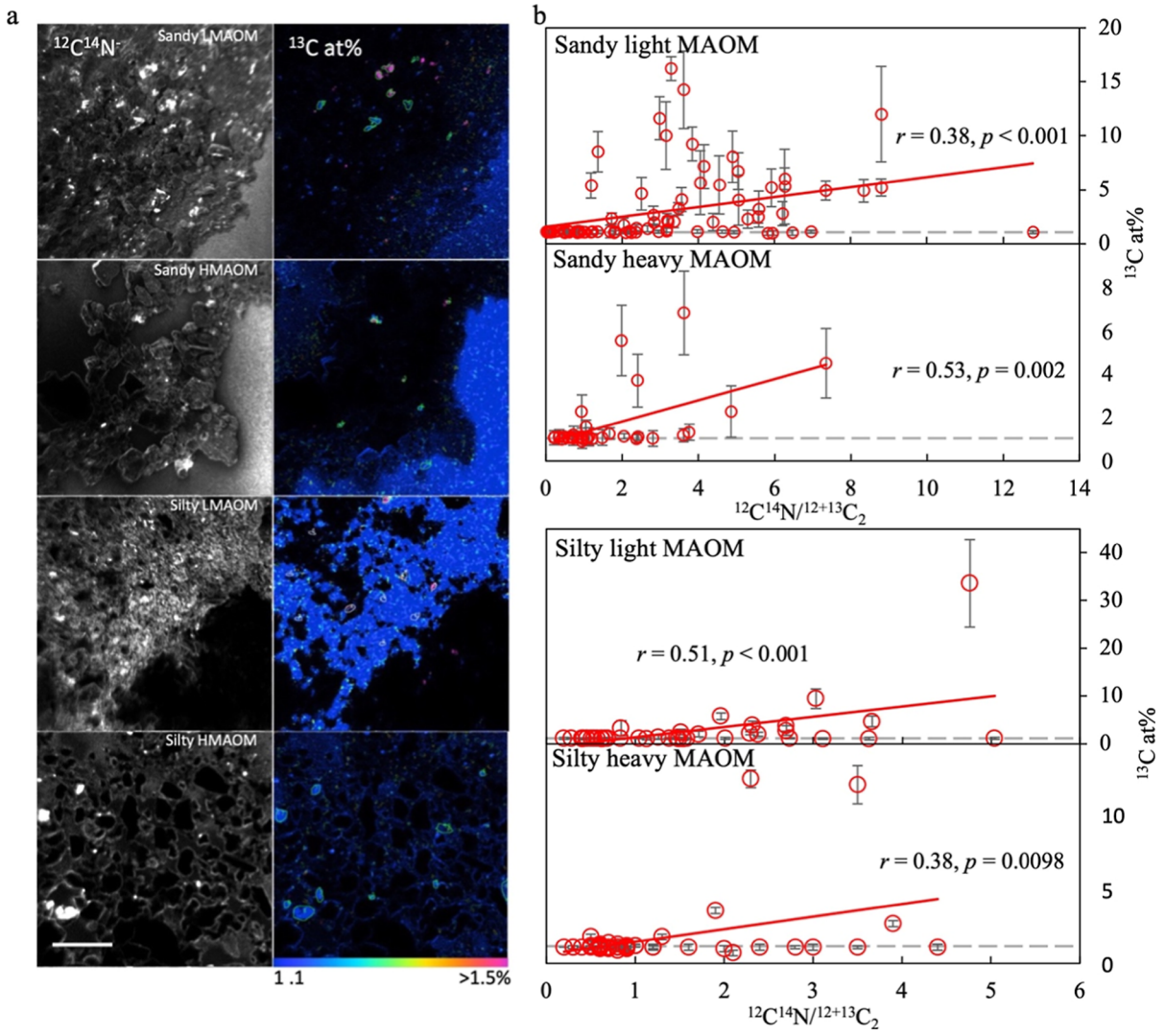

Figure 5. (a) Representative NanoSIMS images for ^{13}C spatial distributions in light and heavy MAOM fractions of sandy and silty soils. The scale bar size is 10 μm. (b) The correlations between ^{13}C atom % and $^{12}C^{14}N/^{12+13}C_2$ ratio of all ROIs from multiple areas of each sample. The dashed line represents $\delta^{13}C = -20‰$ as a representative of the natural abundance of ^{13}C stable isotope. The solid lines represent regression lines including enriched data from all ROIs. These data represent ROIs from multiple areas of NanoSIMS scans for sandy and silty loam soils.

Figures 4a,b and Supplementary Figure S5). For both sandy and silty loams, the light MAOM fraction contains relatively higher abundances of poorly crystalline Fe mineral phases, including nanosize goethite, ferrihydrite, and Fe-OM complexes, whereas the heavy MAOM fraction is relatively more abundant with well-ordered crystalline minerals. In particular, the light MAOM fraction had 3.2 (silty loam) and 2.2 (sandy loam) times the Fe content of poorly crystalline Fe phases (Gt_2 + Fh) compared to the heavy MAOM fraction (Figures 4b and Supplementary Figure S5, more details of Mössbauer spectroscopy results in Supporting Information Note 1). By contrast, the heavy MAOM fraction contains 2.4 (silty loam) and 2.1 (sandy loam) times the proportion of crystalline Fe phases (the sum of Hm and Im) compared to the light MAOM fraction (Supplementary Figure S5); however, the heavy MAOM fraction had only 7 (sandy loam) and 10% (silty loam) higher Fe content of crystalline Fe phases than the light MAOM fraction in sandy and silty loam, respectively. It suggests that although the heavy MAOM fraction does not have much more crystalline Fe minerals in term of Fe content, the heavy MAOM fraction has a significant greater proportion of crystalline Fe minerals than the light MAOM fraction in both soils. The total Fe contents are comparable between sandy loam and silty loam but different between two MAOM fractions in this study. Silty loam light and heavy MAOM contain 43.33 and 20.0 mg of Fe/g of soil, respectively; sandy loam light and heavy MAOM have 41.73 and 20.91 mg of Fe/g of soil, respectively (Supplementary Table S1).

XRD patterns of the heavy MAOM fractions were dominated by quartz (Figure 4c) and contained smaller quantities of feldspar, pyroxene, mica, amphibole, and serpentine (Supplementary Figure S6). The light MAOM fractions are compared with their heavy counterparts in Supplementary Figures S7 and S8. The light fractions contain substantially less crystalline minerals and exhibit a higher background from amorphous material (e.g., organic matter and amorphous Fe-bearing minerals), consistent with the Mössbauer results. Further details of the XRD results are given in Supplementary Note 2. Given the substantial microbial necromass C recovered in the light MAOM fraction, the mineralogical results support microbial necromass accrual and persistence coinciding with poorly crystalline Fe minerals,

https://doi.org/10.1021/acs.est.5c01482
Environ. Sci. Technol. XXXX, XXX, XXX−XXX

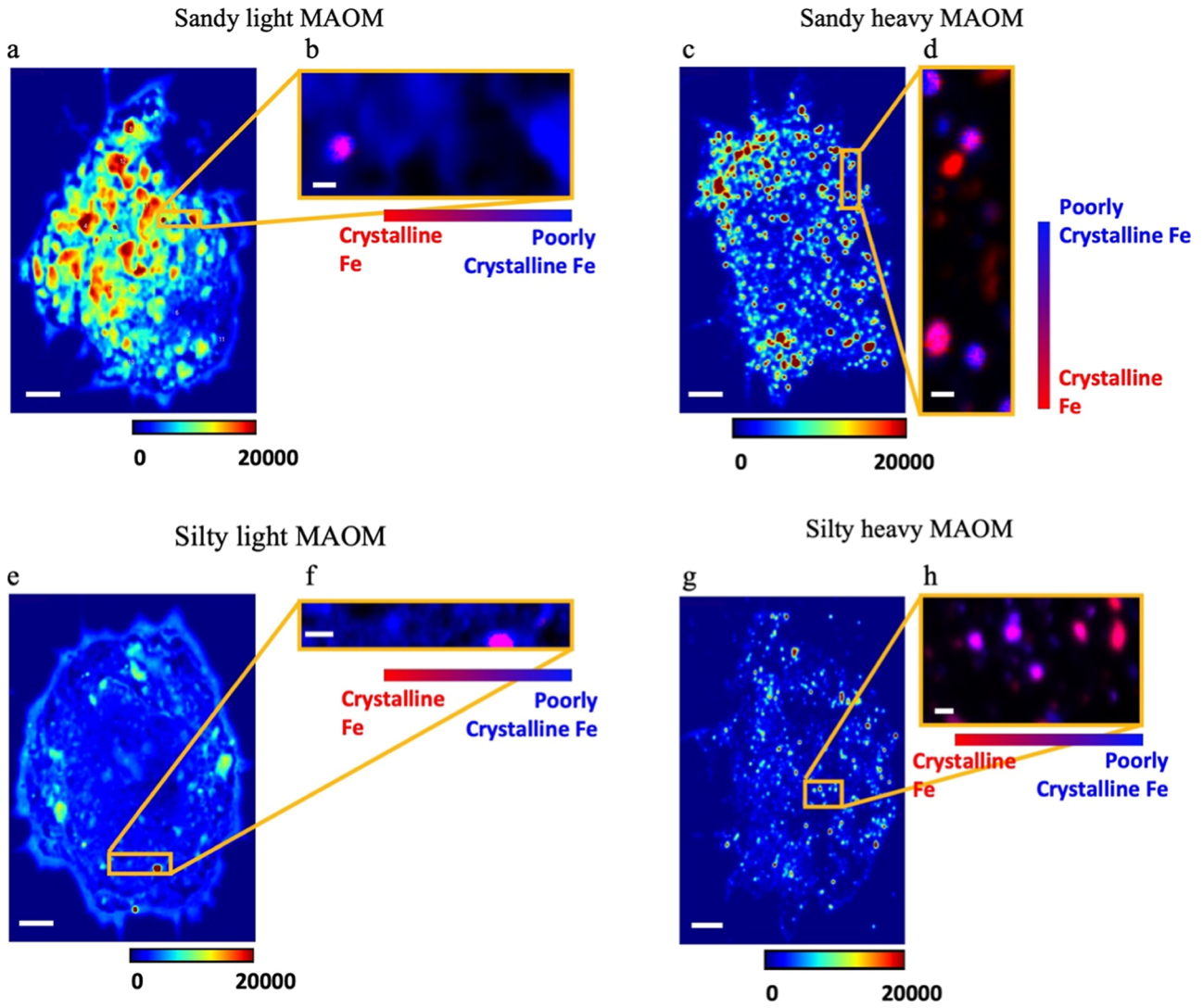

Figure 6. Distributions of total Fe measured on μXRF from (a) sandy light MAOM, (c) sandy heavy MAOM, (e) silty light MAOM, and (g) silty heavy MAOM. Scale bars are 200 μm in (a,c,e,g). Color intensity bars represent total counts of Fe, all scaled to the same maximum intensity for comparison. The high-resolution images of crystalline and poorly crystalline Fe mineral distributions from (b) sandy light MAOM, (d) sandy heavy MAOM, (f) silty light MAOM, and (h) silty heavy MAOM. Scale bars are 20 μm in (b,d,h) and 40 μm in (f). All four samples were from switchgrass samples with no replication given the limited resources (N = 1).

including ferrihydrite and nanosize goethite, and disordered clay minerals in both sandy and silty soils in this study.

3.3. Spatial Distributions of Microbial Necromass and Minerals. NanoSIMS imaging (of CN^- ion yield and ^{13}C enrichment) revealed a greater abundance of microbial necromass hotspots in the light MAOM fraction compared to that in the heavy MAOM fraction for both sandy and silty soils in this study (Figure 5a). The light MAOM fractions from both soils showed a greater number of ^{13}C-rich hotspots than in the heavy MAOM fractions. Spatial distributions of highly enriched microbial residues in the light MAOM fractions are consistent with the mass distribution of microbial derived ^{13}C (Figure 2a), where we found that the quantity of microbial necromass dominated in the light MAOM fraction. There were significantly positive correlations between ^{13}C enrichments (as ^{13}C atomic %) and CN/C_2 ratios (as $^{12}C^{14}N/^{12+13}C_2$) of all ROIs in both light and heavy MAOM fractions from both soils after one year of incubation (Figure 5b). The amount of accumulated ^{13}C increased with the N content, which clearly provides evidence for the accumulation of microbial residues coinciding with the enrichment of ^{13}C in the light MAOM fraction. Aligning well with our XPS results, microbial residues with a higher abundance of N-containing functional groups accrued in the light MAOM fraction via amorphous mineral associations.

The spatial distributions of isotopically labeled microbial necromass were accompanied by variations in Fe mineral distributions between the light and heavy MAOM fractions. μXRF images show the spatial distributions of total Fe as well as two Fe mineral phases for both light MAOM and heavy MAOM fractions (Figure 6). In both soils, the total Fe distribution in the light MAOM fraction is well dispersed, providing large areas for adsorbing and accruing microbial necromass (Figure 6a,e). However, the total Fe distribution in the heavy MAOM fraction is aggregated, forming Fe-rich hotspots (Figure 6c,g). Moreover, in both soils, the light MAOM fraction has well-dispersed distributions of poorly crystalline Fe mineral phases, most likely ferrihydrite (Figure 5b,f); whereas the heavy MAOM fraction is dominated by aggregated crystalline Fe mineral phases, including hematite,

https://doi.org/10.1021/acs.est.5c01482
Environ. Sci. Technol. XXXX, XXX, XXX−XXX

ilmenite, and Fe in clay minerals (Figure 6d,h). Although only one sample was measured per site and per fraction, we ensure distinct Fe spatial distributions between light and heavy MAOM fractions with two soils as replications given the limited resources and highly similar Fe distributions between two soils.

4. DISCUSSION

4.1. Soil Texture Driven Microbial Necromass Retention. Overall, silty loam had a greater accumulation of microbial necromass (μg ^{13}C excess/g soil) compared to sandy loam after one year of incubation, specifically in the light MAOM fraction (Figure 2b). Our results align with previous findings that bulk C accumulation is positively correlated with silt and clay content, whose fine particles and reactive minerals offer large surface area and active sites for stabilizing microbial necromass.[23,55,56] By contrast, the sandy loam had a greater proportion of total C comprised of new microbial necromass compared to the silty loam in this study, as evidenced by the greater ^{13}C excess mass relative to native C (μg ^{13}C excess/mg C) in the MAOM fractions (Supplementary Figure S2b). The greater native C content accounts for the smaller ^{13}C excess mass in total C mass basis (μg of ^{13}C excess/mg of C) in the silty loam. Therefore, our study suggests that although the sandy loam has greater capacity to accumulate microbial necromass per unit of native C, the silty loam has overall greater capacity to accumulate microbial necromass per unit of soil mass due to its higher proportion of fine particles and minerals. We acknowledge that microbial necromass derived from ^{13}C labeled glucose used in this study accounted for only 0.26% of native C, on average, across all fractions, soils, and cropping systems (Supplementary Figure S2b). However, this reflects a one-time C input during a year-long incubation, and microbial residues can accumulate progressively over time. Furthermore, the presence of native C already occupying mineral surfaces may have limited the adsorption of newly produced microbial residues, particularly in the light MAOM fraction. Therefore, our results provide a conservative estimate of the potential contributions of microbial residues to the SOC at our research sites.

Native C concentrations and the availability of reactive sites from mineral surfaces influence C accumulation and the potential for C saturation of the MAOM fraction.[23,26,61] For instance, C-rich soils may have less potential for accruing additional mineral-associated C, whereas C-poor soils have higher potential for additional C as long as they are far below the saturation of active sites.[24,26,61] Here, we estimated C saturation for our two soils according to the average of estimated mineral adsorption capacities from 1144 data points in Georgiou et al.[26] The light MAOM fraction contains 6.56 ± 0.99 wt % of total C in sandy loam and 5.38 ± 0.35 wt % in silty loam (Supplementary Figure S2a), both do not exceed C saturation (19.8 ± 3.2 wt % for sandy loam, 23.0 ± 5.6 wt % for silty loam, Supplementary Figure S3). Therefore, the lower ^{13}C enrichment relative to native C in the silty loam likely reflects dilution by higher native C and greater pre-existing coverage of mineral surfaces.

In this study, ^{13}C glucose was added as a highly bioavailable substrate and may not fully capture the transformation and stabilization dynamics of the more chemically complex OM received from the field. Previous studies demonstrated that microbial C use efficiency and necromass composition vary with substrate quality, affecting its retention by reactive mineral surfaces. In particular, labile C promotes necromass accumulation with MAOM in microbial hotspots (e.g., rhizosphere), whereas more complex inputs may sorb directly to minerals or be stabilized via aggregation pathways.[5,6] Future studies are needed to investigate microbial residue dynamics under a wider range of substrates to capture these alternative stabilization processes. Although the type of C sources affects metabolite composition and SOM persistence,[62] ecosystem-level factors, including climate, microbial community composition, and soil properties, have a stronger influence on SOM dynamics and microbial contributions to C cycling.[63]

4.2. Mineral-Mediated Persistence of Microbial Necromass C. A quantitative assessment revealed that poorly crystalline Fe minerals are key in accruing microbial necromass. For bulk SOC, mineralogy, e.g., Fe and Al (hydro)oxides, is considered a dominant driver of SOC persistence,[11,15,20,64] with MAOM fractions contributing up to 72% of total SOC across ecosystems.[20,64,65] Poorly crystalline or amorphous Fe (hydro)oxides, due to their high surface area and reactivity, are preferentially responsible for soil C persistence compared with crystalline Fe (hydro)oxides. For the microbial portion of bulk SOC, while microbial necromass sorption to synthetic amorphous Al hydroxide has been shown,[8] and microbial residues are known to dominate MAOM in artificial soils,[66] their association with specific mineral phases in native soils has not been quantified. Using XRD and ^{57}Fe−Mössbauer spectroscopy, our study provides novel evidence of contrasting mineral composition between light and heavy MAOM fractions while showing consistency in mineral phases across both soil types. These findings highlight the power of amorphous minerals to retain microbial necromass with substantial ^{13}C accumulation observed in MAOM fractions, particularly the light MAOM fraction in our study, regardless of soil texture. We recognize that soil texture covaries with other properties, including mineralogy, suggesting that both texture and mineralogy jointly influence micrbial necromass accumulation across sites. However, by coupling a quantitative assessment of microbial necromass C with characterizations of soil mineralogy within a given soil, this study demonstrated that mineralogy plays the primary role in regulating microbial necromass accumulation across different SOM pools. The mineral-mediated microbial necromass accumulation is therefore fundamental to soil management approaches and policies focused on predictions of soil C sequestration potential of diverse soils.

By differentiating light and heavy MAOM fractions, our study shows a great potential for optimizing process-based models, such as Microbial-Mineral Caron Stabilization (MIMICS),[67] to understand and predict microbial necromass contributions to SOM pools. Parametric uncertainty caused the physicochemically protected SOM pool to vary by an average factor of 4.4 across individual watershed locations (e.g., 10 − 44 kg C/m^2), underscoring the need for additional measurements of protected SOM pool sizes and their turnover time to improve confidence in the MIMICS simulations of SOC dynamics.[67] Our study demonstrates that the light MAOM fraction largely represents the physicochemical protection of microbial necromass and SOC in soil. By considering differentiating light and heavy MAOM fractions in soil pool measurements, we may improve the confidence in the MIMICS simulations and other process-based model simulations predicting microbial necromase contributions to SOM pools.

https://doi.org/10.1021/acs.est.5c01482
Environ. Sci. Technol. XXXX, XXX, XXX−XXX

4.3. Spatially Explicit Accumulation of Microbial Necromass. Poorly crystalline Fe minerals accrue microbial necromass in spatially distinct regions due to the chemical functionality of microbial necromass compounds and mineral surfaces. Regardless of soil texture, μ-XRF mapping indicates that the light MAOM fraction was dominated by widely distributed poorly crystalline Fe minerals. The greater ^{13}C accumulation in the light MAOM fraction (Figure 2) is explained by the well dispersed poorly crystalline Fe minerals (Figure 6) and ^{13}C labeled microbial residues (Figure 5). Spatially dispersed poorly crystalline Fe minerals create a reactive surface area that is conducive to C accrual. In contrast, crystalline Fe mineral hot spots that are evident in the heavy fraction accumulated less microbial necromass, perhaps due to the lower overall mineral content and smaller area of reactive surfaces compared to poorly crystalline minerals.

The light MAOM fraction was enriched in ^{13}C labeled microbial necromass and had a higher amount of carboxylic C- and N-containing functional groups than the heavy MAOM fraction. The carboxylic C and N-rich functional groups have been found to bond to mineral surfaces. The enriched hydroxyl groups on ferrihydrite surfaces, a representative of poorly crystalline Fe hydroxides, interact with carboxylic groups via H bond or cation bridging.[68] Previous studies found that N-rich microbial-derived molecules strongly attach to mineral surfaces from natural soils.[18,19,69] Moreover, carboxylic fractions were found to be preferentially associated with poorly crystalline minerals in bulk soils.[20−22] But none of these studies have isolated the microbial necromass-specific pool and investigated bonding interactions from microbial necromass and poorly crystalline Fe minerals in soil. Our research demonstrates the importance of dispersed amorphous mineral surfaces for binding microbial residues rich in carboxylic and amide functional groups. Together, such microbe−mineral interactions form necromass-rich MAOM that can persist over time and is resistant to release with repeated wet−dry cycles. The current work cannot spatially correlate distributions of microbial necromass and poorly crystalline Fe minerals due to different spatial resolutions between NanoSIMS and μ-XRF approaches; future research could address such spatial correlations with other imaging techniques. For instance, mass spectrometry imaging (MSI) could map chemical features of microbial necromass and couple to Fe spatial distributions.

■ ASSOCIATED CONTENT

Supporting Information

The Supporting Information is available free of charge at https://pubs.acs.org/doi/10.1021/acs.est.5c01482.

Mössbauer spectroscopy methods and results; XRD patterns and mineral phase identifications; figures of Fe mineral proportions, carbon and ^{13}C mass distributions, carbon saturation, C/N ratios, modeled Mössbauer spectra, and XRD pattern comparisons; and tables of total Fe, Fe^{2+}/Fe^{3+} concentrations, and Mössbauer spectral parameters (PDF)

■ AUTHOR INFORMATION

Corresponding Author

Kirsten S. Hofmockel − *Environmental and Biological Sciences Directorate, Pacific Northwest National Laboratory, Richland, Washington 99354, United States; Department of Agronomy, Iowa State University, Ames, Iowa 50011, United States;* orcid.org/0000-0003-1586-2167; Phone: +1 (509)371-6444; Email: kirsten.hofmockel@pnnl.gov

Authors

Qian Zhao − *Environmental and Biological Sciences Directorate, Pacific Northwest National Laboratory, Richland, Washington 99354, United States;* Present Address: Q.Z: The University of Texas at Dallas, Richardson, Texas, 75080, United States; orcid.org/0000-0003-4489-3691

Sheryl Bell − *Environmental and Biological Sciences Directorate, Pacific Northwest National Laboratory, Richland, Washington 99354, United States*

Ravi Kukkadapu − *Environmental and Biological Sciences Directorate, Pacific Northwest National Laboratory, Richland, Washington 99354, United States*

Jocelyn Richardson − *Stanford Synchrotron Radiation Lightsource, SLAC National Accelerator Laboratory, Menlo Park, California 94025, United States*

John Cliff − *Environmental and Biological Sciences Directorate, Pacific Northwest National Laboratory, Richland, Washington 99354, United States; National Security Sciences Directorate, Oakridge National Laboratory, Oak Ridge, Tennessee 37830, United States*

Mark Bowden − *Environmental and Biological Sciences Directorate, Pacific Northwest National Laboratory, Richland, Washington 99354, United States;* orcid.org/0000-0003-3812-3340

Sarah Leichty − *Environmental and Biological Sciences Directorate, Pacific Northwest National Laboratory, Richland, Washington 99354, United States*

Complete contact information is available at: https://pubs.acs.org/10.1021/acs.est.5c01482

Author Contributions

Q.Z., S.B., and K.S.H. conceived the study. Q.Z. and K.S.H. wrote the manuscript. S.B., R.K., J.R., J.C., and S.L. reviewed and edited the manuscript. Q.Z. and S.B. performed the isotope incubation experiments. Q.Z. and S.L. performed the density fractionation experiment. Q.Z., S.B., R.K., J.R., J.C., and M.B. performed the characterization analyses and data analysis. K.S.H. obtained funding.

Notes

The authors declare no competing financial interest.

■ ACKNOWLEDGMENTS

This research was supported by an Early Career Research Program award funded by the U.S. Department of Energy (DOE), Office of Science, Office of Biological and Environmental Research (BER) Genomic Science program under FWP 68292 and FWP 07880, Environmental Molecular Sciences Laboratory (EMSL) Exploratory Research Project 51095, and Stanford Synchrotron Radiation Lightsource (SSRL) user proposal S-XV-ST-5898. A portion of this work was performed in EMSL, at Pacific Northwest National Laboratory (PNNL). PNNL is a multiprogram national laboratory operated by Battelle for the DOE under Contract DE-AC05-76RLO 1830. Use of the SSRL, SLAC National Accelerator Laboratory, is supported by the DOE, Office of Science, Office of Basic Energy Sciences under contract DE-AC02-76SF00515. The SSRL Structural Molecular Biology

https://doi.org/10.1021/acs.est.5c01482
Environ. Sci. Technol. XXXX, XXX, XXX−XXX

Program is supported by the DOE-BER and by the National Institutes of Health (NIH), National Institute of General Medical Sciences (NIGMS; P30GM133894). The contents of this publication are solely the responsibility of the authors and do not necessarily represent the official views of the NIGMS or the NIH. J.R. is supported by supplemental funding from DOE-BER to assist and expand biological and environmental relevant research and users at SSRL.

■ ABBREVIATIONS

SOM, soil organic matter; C, carbon; SOC, soil organic carbon; MAOM, mineral-associated organic matter; POM, particulate organic matter; DOC, dissolved organic carbon; OM, organic matter; IRMS, isotope ratio mass spectrometry; XRD, X-ray diffraction; NA, natural abundance; NanoSIMS, nanoscale secondary ion mass spectrometry; SEM, scanning electron microscopy; ROI, regions of interest; XRF, X-ray fluorescence; XANES, X-ray absorption near edge structure; SSRL, Stanford synchrotron radiation lightsource; XPS, X-ray photoelectron spectroscopy.

■ REFERENCES

(1) Paustian, K.; Lehmann, J.; Ogle, S.; Reay, D.; Robertson, G. P.; Smith, P. Climate-smart soils. *Nature* **2016**, *532* (7597), 49−57.
(2) Angst, G.; Mueller, K. E.; Nierop, K. G.; Simpson, M. J. Plant-or microbial-derived? A review on the molecular composition of stabilized soil organic matter. *Soil Biol. Biochem.* **2021**, *156*, 108189.
(3) Schmidt, M. W. I.; Torn, M. S.; Abiven, S.; Dittmar, T.; Guggenberger, G.; Janssens, I. A.; Kleber, M.; Kögel-Knabner, I.; Lehmann, J.; Manning, D. A. C.; Nannipieri, P.; Rasse, D. P.; Weiner, S.; Trumbore, S. E. Persistence of Soil Organic Matter as an Ecosystem Property. *Nature* **2011**, *478* (7367), 49−56.
(4) Ma, T.; Zhu, S.; Wang, Z.; Chen, D.; Dai, G.; Feng, B.; Su, X.; Hu, H.; Li, K.; Han, W.; Liang, C.; Bai, Y.; Feng, X. Divergent accumulation of microbial necromass and plant lignin components in grassland soils. *Nat. Commun.* **2018**, *9*, 3480.
(5) Sokol, N. W.; Bradford, M. A. Microbial formation of stable soil carbon is more efficient from belowground than aboveground input. *Nat. Geosci.* **2019**, *12*, 46−53.
(6) Liang, C.; Amelung, W.; Lehmann, J.; Kästner, M. Quantitative assessment of microbial necromass contribution to soil organic matter. *Global Change Biol.* **2019**, *25*, 3578−3590.
(7) Wang, B.; An, S.; Liang, C.; Liu, Y.; Kuzyakov, Y. Microbial necromass as the source of soil organic carbon in global ecosystems. *Soil Biol. Biochem.* **2021**, *162*, 108422.
(8) Creamer, C. A.; Foster, A. L.; Lawrence, C.; McFarland, J.; Schulz, M.; Waldrop, M. P. Mineralogy dictates the initial mechanism of microbial necromass association. *Geochim. Cosmochim. Acta* **2019**, *260*, 161−176.
(9) Kleber, M.; Bourg, I. C.; Coward, E. K.; Hansel, C. M.; Myneni, S. C. B.; Nunan, N. Dynamic interactions at the mineral−organic matter interface. *Nat. Rev. Earth Environ.* **2021**, *2*, 402−421.
(10) Buckeridge, K. M.; Mason, K. E.; Ostle, N.; McNamara, N. P.; Grant, H. K.; Whitaker, J. Microbial necromass carbon and nitrogen persistence are decoupled in agricultural grassland soils. *Commun. Earth Environ.* **2022**, *3*, 114.
(11) Mikutta, R.; Kleber, M.; Torn, M. S.; Jahn, R. Stabilization of soil organic matter: association with minerals or chemical recalcitrance? *Biogeochemistry* **2006**, *77*, 25−56.
(12) Kallenbach, C. M.; Frey, S. D.; Grandy, A. S. Direct evidence for microbial-derived soil organic matter formation and its ecophysiological controls. *Nat. Commun.* **2016**, *7*, 13630.
(13) Kaiser, K.; Guggenberger, G. Mineral surfaces and soil organic matter. *Eur. J. Soil Sci.* **2003**, *54*, 219−236.
(14) Kleber, M.; Eusterhues, K.; Keiluweit, M.; Mikutta, C.; Mikutta, R.; Nico, P. S. Mineral−organic associations: formation, properties, and relevance in soil environments. In *Advances in agronomy*; Sparks, D., Ed.; Elsevier Academic Press Inc., 2015; pp 1−140.
(15) Zhao, Q.; Callister, S. J.; Thompson, A. M.; Kukkadapu, R. K.; Tfaily, M. M.; Bramer, L. M.; Qafoku, N. P.; Bell, S. L.; Hobbie, S. E.; Seabloom, E. W.; Borer, E. T.; Hofmockel, K. S. Strong mineralogic control of soil organic matter composition in response to nutrient addition across diverse grassland sites. *Sci. Total Environ.* **2020**, *736*, 137839.
(16) Wagai, R.; Kajiura, M.; Asano, M. Iron and aluminum association with microbially processed organic matter via meso-density aggregate formation across soils: organo-metallic glue hypothesis. *Soil* **2020**, *6*, 597−627.
(17) Lehmann, J.; Hansel, C. M.; Kaiser, C.; Kleber, M.; Maher, K.; Manzoni, S.; Nunan, N.; Reichstein, M.; Schimel, J. P.; Torn, M. S.; Wieder, W. R.; Kögel-Knabner, I. Persistence of soil organic carbon caused by functional complexity. *Nat. Geosci.* **2020**, *13*, 529−534.
(18) Kopittke, P. M.; Hernandez-Soriano, M. C.; Dalal, R. C.; Finn, D.; Menzies, N. W.; Hoeschen, C.; Mueller, C. W. Nitrogen-rich microbial products provide new organo-mineral associations for the stabilization of soil organic matter. *Global Change Biol.* **2018**, *24*, 1762−1770.
(19) Keiluweit, M.; Bougoure, J. J.; Zeglin, L. H.; Myrold, D. D.; Weber, P. K.; Pett-Ridge, J.; Kleber, M.; Nico, P. S. Nano-scale investigation of the association of microbial nitrogen residues with iron (hydr) oxides in a forest soil O-horizon. *Geochim. Cosmochim. Acta* **2012**, *95*, 213−226.
(20) Zhao, Q.; Poulson, S. R.; Obrist, D.; Sumaila, S.; Dynes, J. J.; McBeth, J. M.; Yang, Y. Iron-bound organic carbon in forest soils: quantification and characterization. *Biogeosciences* **2016**, *13*, 4777−4788.
(21) Coward, E. K.; Ohno, T.; Plante, A. F. Adsorption and molecular fractionation of dissolved organic matter on iron-bearing mineral matrices of varying crystallinity. *Environ. Sci. Technol.* **2018**, *52*, 1036−1044.
(22) Zhang, Y.; Lavallee, J. M.; Robertson, A. D.; Even, R.; Ogle, S. M.; Paustian, K.; Cotrufo, M. F. Simulating measurable ecosystem carbon and nitrogen dynamics with the mechanistically defined MEMS 2.0 model. *Biogeosciences* **2021**, *18*, 3147−3171.
(23) Six, J.; Conant, R. T.; Paul, E. A.; Paustian, K. Stabilization mechanisms of soil organic matter: Implications for C-saturation of soils. *Plant Soil* **2002**, *241*, 155−176.
(24) Cotrufo, M. F.; Ranalli, M. G.; Haddix, M. L.; Six, J.; Lugato, E. Soil carbon storage informed by particulate and mineral-associated organic matter. *Nat. Geosci.* **2019**, *12*, 989−994.
(25) Lavallee, J. M.; Soong, J. L.; Cotrufo, M. F. Conceptualizing soil organic matter into particulate and mineral-associated forms to address global change in the 21st century. *Global Change Biol.* **2020**, *26*, 261−273.
(26) Georgiou, K.; Jackson, R. B.; Vindušková, O.; Abramoff, R. Z.; Ahlström, A.; Feng, W.; Harden, J. W.; Pellegrini, A. F. A.; Polley, H. W.; Soong, J. L.; Riley, W. J.; Torn, M. S. Global stocks and capacity of mineral-associated soil organic carbon. *Nat. Commun.* **2022**, *13*, 3797.
(27) Sollins, P.; Swanston, C.; Kleber, M.; Filley, T.; Kramer, M.; Crow, S.; Caldwell, B. A.; Lajtha, K.; Bowden, R. Organic C and N stabilization in a forest soil: evidence from sequential density fractionation. *Soil Biol. Biochem.* **2006**, *38*, 3313−3324.
(28) Sollins, P.; Kramer, M. G.; Swanston, C.; Lajtha, K.; Filley, T.; Aufdenkampe, A. K.; Wagai, R.; Bowden, R. D. Sequential density fractionation across soils of contrasting mineralogy: evidence for both microbial-and mineral-controlled soil organic matter stabilization. *Biogeochemistry* **2009**, *96*, 209−231.
(29) Hatton, P. J.; Kleber, M.; Zeller, B.; Moni, C.; Plante, A. F.; Townsend, K.; Gelhaye, L.; Lajtha, K.; Derrien, D. Transfer of litter-derived N to soil mineral−organic associations: evidence from decadal ^{15}N tracer experiments. *Org. Geochem.* **2012**, *42*, 1489−1501.
(30) Crow, S. E.; Lajtha, K.; Filley, T. R.; Swanston, C. W.; Bowden, R. D.; Caldwell, B. A. Sources of plant-derived carbon and stability of

https://doi.org/10.1021/acs.est.5c01482
Environ. Sci. Technol. XXXX, XXX, XXX−XXX

organic matter in soil: Implications for global change. *Global Change Biol.* **2009**, *15*, 2003−2019.
(31) Samson, M. E.-; Chantigny, M. H.; Vanasse, A.; Menasseri-Aubry, S.; Angers, D. A. Coarse mineral-associated organic matter is a pivotal fraction for SOM formation and is sensitive to the quality of organic inputs. *Soil Biol. Biochem.* **2020**, *149*, 107935.
(32) Jesus, E. d. C.; Liang, C.; Quensen, J. F.; Susilawati, E.; Jackson, R. D.; Balser, T. C.; Tiedje, J. M. Influence of corn, switchgrass, and prairie cropping systems on soil microbial communities in the upper Midwest of the United States. *GCB Bioenergy* **2016**, *8*, 481−494.
(33) Kasanke, C. P.; Zhao, Q.; Bell, S.; Thompson, A. M.; Hofmockel, K. S. Can switchgrass increase carbon accrual in marginal soils? The importance of site selection. *GCB Bioenergy* **2021**, *13*, 320−335.
(34) Web Soil Survey. National Cooperate Soil Survey, https://websoilsurvey.sc.egov.usda.gov/app/WebSoilSurvey.aspx (accessed 12 18, 2023).
(35) Muñoz, J. D.; Kravchenko, A. Soil carbon mapping using on-the-go near infrared spectroscopy, topography and aerial photographs. *Geoderma* **2011**, *166*, 102−110.
(36) Sanford, G. R.; Oates, L. G.; Jasrotia, P.; Thelen, K. D.; Robertson, G. P.; Jackson, R. D. Comparative productivity of alternative cellulosic bioenergy cropping systems in the North Central USA. *Agric., Ecosyst. Environ.* **2016**, *216*, 344−355.
(37) Blagodatskaya, E.; Yuyukina, T.; Blagodatsky, S.; Kuzyakov, Y. Turnover of soil organic matter and of microbial biomass under C3−C4 vegetation change: Consideration of ^{13}C fractionation and preferential substrate utilization. *Soil Biol. Biochem.* **2011**, *43*, 159−166.
(38) (a) Kuzyakov, Y.; Blagodatskaya, E.; Blagodatsky, S.; Kemmitt, S. J.; Lanyon, C. V.; Waite, I. S.; Wen, Q.; Addiscott, T. M.; Bird, N. R. A.; O'Donnell, A. G.; Brookes, P. C. Mineralization of native soil organic matter is not regulated by the size, activity or composition of the soil microbial biomass − A new perspective. *Soil Biol. Biochem.* **2008**, *40*, 61−73. (b) Kuzyakov, Y.; Blagodatskaya, E.; Blagodatsky, S.; Kemmitt, S. J.; Lanyon, C. V.; Waite, I. S.; Wen, Q.; Addiscott, T. M.; Bird, N. R. A.; O'Donnell, A. G.; Brookes, P. C. The biology of the Regulatory Gate. *Soil Biol. Biochem.* **2009**, *41*, 435−439.
(39) Rempfert, K. R.; Bell, S. L.; Kasanke, C. P.; Zhao, Q.; Zhao, X.; Lipton, A. S.; Hofmockel, K. S. Biomolecular budget of persistent, microbial-derived soil organic carbon: The importance of underexplored pools. *Sci. Total Environ.* **2024**, *932*, 172916.
(40) Tiemann, L. K.; Billings, S. A. Changes in variability of soil moisture alter microbial community C and N resource use. *Soil Biol. Biochem.* **2011**, *43*, 1837−1847.
(41) Zhao, Q.; Thompson, A. M.; Callister, S. J.; Tfaily, M. M.; Bell, S. L.; Hobbie, S. E.; Hofmockel, K. S. Dynamics of organic matter molecular composition under aerobic decomposition and their response to the nitrogen addition in grassland soils. *Sci. Total Environ.* **2022**, *806*, 150514.
(42) Viret, F.; Grand, S. Combined size and density fractionation of soils for investigations of organo-mineral interactions. *J. Vis. Exp.* **2019**, No. e58927.
(43) Coplen, T. B.; Brand, W. A.; Gehre, M.; Gröning, M.; Meijer, H. A.; Toman, B.; Verkouteren, R. M. New guidelines for $\delta^{13}C$ measurements. *Anal. Chem.* **2006**, *78*, 2439−2441.
(44) Peretyazhko, T. S.; Zachara, J. M.; Kukkadapu, R. K.; Heald, S. M.; Kutnyakov, I. V.; Resch, C. T.; Arey, B. W.; Wang, C. M.; Kovarik, L.; Phillips, J. L.; Moore, D. A. Pertechnetate (TcO^{4-}) reduction by reactive ferrous iron forms in naturally anoxic, redox transition zone sediments from the Hanford Site, USA. *Geochim. Cosmochim. Acta* **2012**, *92*, 48−66.
(45) Rancourt, D. G.; Ping, J. Y. Voigt-based methods for arbitrary-shape static hyperfine parameter distributions in Mössbauer spectroscopy. *Nucl. Instrum. Methods Phys. Res., Sect. B* **1991**, *58*, 85−97.
(46) Mueller, C. W.; Kölbl, A.; Hoeschen, C.; Hillion, F.; Heister, K.; Herrmann, A. M.; Kögel-Knabner, I. Submicron scale imaging of soil organic matter dynamics using NanoSIMS−from single particles to intact aggregates. *Org. Geochem.* **2012**, *42*, 1476−1488.
(47) Mayhew, L.; Webb, S.; Templeton, A. Microscale imaging and identification of Fe speciation and distribution during fluid−mineral reactions under highly reducing conditions. *Environ. Sci. Technol.* **2011**, *45*, 4468−4474.
(48) Webb, S. M. SIXpack: a graphical user interface for XAS analysis using IFEFFIT. *Phys. Scr.* **2005**, *2005*, 1011.
(49) Ravel, B.; Newville, M. ATHENA and ARTEMIS: interactive graphical data analysis using IFEFFIT. *Phys. Scr.* **2005**, *2005*, 1007.
(50) Webb, S. M. The MicroAnalysis Toolkit: X-ray fluorescence image processing software. *AIP Conf. Proc.* **2011**, *1365* (1), 196−199.
(51) Huang, Y. L.; Tien, H. W.; Ma, C. C. M.; Yang, S. Y.; Wu, S. Y.; Liu, H. Y.; Mai, Y. W. Effect of extended polymer chains on properties of transparent graphene nanosheets conductive film. *J. Mater. Chem.* **2011**, *21*, 18236−18241.
(52) Cheng, C. H.; Lehmann, J.; Thies, J. E.; Burton, S. D.; Engelhard, M. H. Oxidation of black carbon by biotic and abiotic processes. *Org. Geochem.* **2006**, *37*, 1477−1488.
(53) Proctor, A.; Sherwood, P. M. A. X-ray photoelectron spectroscopic studies of carbon fibre surfaces. III—Industrially treated fibres and the effect of heat and exposure to oxygen. *Surf. Interface Anal.* **1982**, *4*, 212−219.
(54) Six, J.; Doetterl, S.; Laub, M.; Müller, C. R.; Van de Broek, M. The six rights of how and when to test for soil C saturation. *Soil* **2024**, *10*, 275−279.
(55) Feng, W.; Plante, A. F.; Six, J. Improving estimates of maximal organic carbon stabilization by fine soil particles. *Biogeochemistry* **2013**, *112*, 81−93.
(56) Matus, F. J. Fine silt and clay content is the main factor defining maximal C and N accumulations in soils: a meta-analysis. *Sci. Rep.* **2021**, *11*, 6438.
(57) Salonen, A. R.; de Goede, R.; Creamer, R.; Heinonsalo, J.; Soinne, H. Soil organic carbon fractions and storage potential in F innish arable soils. *Eur. J. Soil Sci.* **2024**, *75*, No. e13527.
(58) R Core Team. *R: A Language and Environment for Statistical Computing*; R Foundation for Statistical Computing. https://www.R-project.org/(accessed 2024−02−04).
(59) Cava, F.; Lam, H.; De Pedro, M. A.; Waldor, M. K. Emerging knowledge of regulatory roles of D-amino acids in bacteria. *Cell. Mol. Life Sci.* **2011**, *68*, 817−831.
(60) Amelung, W.; Blume, H. P.; Fleige, H.; Horn, R.; Kandeler, E.; Kögel-Knabner, I.; Kretzschmar, R.; Stahr, K.; Wilke, B. M. *Scheffer/Schachtschabel Lehrbuch Der Bodenkunde*; Springer-Verlag, 2018.
(61) Stewart, C. E.; Paustian, K.; Conant, R. T.; Plante, A. F.; Six, J. Soil carbon saturation: concept, evidence and evaluation. *Biogeochemistry* **2007**, *86*, 19−31.
(62) Wilhelm, R. C.; Barnett, S. E.; Swenson, T. L.; Youngblut, N. D.; Koechli, C. N.; Bowen, B. P.; Northen, T. R.; Buckley, D. H. Tracing carbon metabolism with stable isotope metabolomics reveals the legacy of diverse carbon sources in soil. *Appl. Environ. Microbiol.* **2022**, *88*, No. e0083922.
(63) Throckmorton, H. M.; Bird, J. A.; Dane, L.; Firestone, M. K.; Horwath, W. R. The source of microbial C has little impact on soil organic matter stabilisation in forest ecosystems. *Ecol. Lett.* **2012**, *15*, 1257−1265.
(64) Wagai, R.; Mayer, L. M. Sorptive stabilization of organic matter in soils by hydrous iron oxides. *Geochim. Cosmochim. Acta* **2007**, *71*, 25−35.
(65) Lalonde, K.; Mucci, A.; Ouellet, A.; Gélinas, Y. Preservation of organic matter in sediments promoted by iron. *Nature* **2012**, *483*, 198−200.
(66) Wang, X.; Wang, C.; Fan, X.; Sun, L.; Sang, C.; Wang, X.; Jiang, P.; Fang, Y.; Bai, E. Mineral composition controls the stabilization of microbially derived carbon and nitrogen in soils: Insights from an isotope tracing model. *Global Change Biol.* **2024**, *30*, No. e17156.
(67) Pierson, D.; Lohse, K. A.; Wieder, W. R.; Patton, N. R.; Facer, J.; de Graaff, M. A.; Georgiou, K.; Seyfried, M. S.; Flerchinger, G.; Will, R. Optimizing process-based models to predict current and future soil organic carbon stocks at high-resolution. *Sci. Rep.* **2022**, *12*, 10824.

https://doi.org/10.1021/acs.est.5c01482
Environ. Sci. Technol. XXXX, XXX, XXX−XXX

(68) Lützow, M. V.; Kögel-Knabner, I.; Ekschmitt, K.; Matzner, E.; Guggenberger, G.; Marschner, B.; Flessa, H. Stabilization of organic matter in temperate soils: mechanisms and their relevance under different soil conditions − a review. *Eur. J. Soil Sci.* **2006**, *57*, 426−445.
(69) Possinger, A. R.; Zachman, M. J.; Enders, A.; Levin, B. D.; Muller, D. A.; Kourkoutis, L. F.; Lehmann, J. Organo−organic and organo−mineral interfaces in soil at the nanometer scale. *Nat. Commun.* **2020**, *11*, 6103.

https://doi.org/10.1021/acs.est.5c01482
Environ. Sci. Technol. XXXX, XXX, XXX−XXX